Geophys. J. Int. (2003) **154,** 117–133

Combined traveltime and frequency-domain seismic waveform inversion: a case study on multi-offset ultrasonic data

J.-X. Dessa[1] and G. Pascal[2]

[1] *Géosciences Azur, OOV, CNRS UMR* 652, *La Darse BP* 48, 06235 *Villefranche-sur-Mer, France. E-mail: jxdessa@obs.vlfr.fr*
[2] *Laboratoire de Géologie, École Normale Supérieure, UMR* 8536, 75231 *Paris, France*

Accepted 2003 January 31. Received 2003 January 31; in original form 2001 May 18

SUMMARY

We present the acquisition and processing of a multi-offset ultrasonic tomography experiment in which we aim to precisely reconstruct the image and kinematic properties of two scatterers that contrast strongly with the water background. The resultant non-linearity causes the failure of a frequency-domain waveform fitting strategy for retrieving the whole range of experimentally covered wavenumbers. A mixed tomographic approach is instead adopted in which traveltime and waveform inversion are combined iteratively. This strategy helps in overcoming the waveform inverse problem non-linearity and the data computed in our final tomographic model match most of the observed features in the experimental seismograms. This model is in good agreement with what is known concerning the properties of the scatterers and it is characterized by both the high focusing of waveform tomography and the accurate kinematics of traveltime tomography. These achievements are reached in spite of a limited, but nevertheless uniform, geometric coverage. Our strategy of using two different tomographic tools sequentially therefore appears to be a possible solution to addressing the issue of highly non-linear seismic inverse problems.

Key words: combined tomography, frequency-domain waveform inversion, non-linear inverse problem, traveltime inversion, ultrasonic data, wavenumber coverage.

1 INTRODUCTION

In seismic waveform inversion, all of the information contained in recorded seismograms is used to retrieve physical properties that are relevant to seismic wave propagation in a zone of study. Used in combination with a modelling technique that has the ability to simulate every aspect of the behaviour of the wavefield, such a method theoretically allows one to obtain a model of the area that should only be limited by the properties of the acquisition device (positions of sources and receivers, bandwidth of the signal). Important studies on the application of waveform inversion techniques in the seismic imaging and seismic tomography problems have been achieved over the last two decades on both theoretical and numerical aspects, the latter being greatly favoured by the developments in available computational resources that made realistic applications more and more feasible.

Theoretical studies have provided a framework for the implementation of the seismic waveform inverse problem with an increasing degree of complexity. First of all, it was demonstrated that the local linearized approach of the inverse problem could be seen as a sequence of pre-stack depth migrations (Lailly 1984; Tarantola 1984). The acoustic (Tarantola 1984), elastic (Tarantola 1986) and viscoelastic (Tarantola 1988) cases were subsequently described. On the other hand, numerical implementations were carried out on synthetic (Gauthier *et al.* 1986; Mora 1987, 1988; Crase *et al.* 1990) and real data sets (Crase *et al.* 1990, 1992; Igel *et al.* 1996; Djikpesse & Tarantola 1999).

The studies cited above used a modelling tool based on a finite-difference resolution of the wave equation in the space–time domain, which will be simply quoted as the (**r**, t) domain or time domain hereafter. However, seismic wave modelling by finite differences can be equivalently carried out in the (**r**, ω) (for space–frequency) domain (Marfurt 1984), with great potential benefit when numerous sources are involved, as is usual in seismic sounding experiments.

Instead of just limiting the modelling to the (**r**, ω) domain and computing time seismograms using an inverse Fourier transform, it is quite worthwhile to also implement the inverse problem in this domain. First, it can be shown that a complete wavenumber coverage of the model (to the extent of the source frequency bandwidth) can be achieved with a limited number of frequencies, particularly when wide aperture data are considered (Devaney 1984; Wu & Toksöz 1987; Pratt & Worthington 1990). This can lead to a huge decimation in the volume of data to invert and therefore, to a strong decrease in the computational resources required to do so. Besides this, performing the inversion in the (**r**, ω) domain easily allows an iterative processing of the signal with increasing frequencies. To some extent, this strategy can limit the strong non-linearity of the seismic waveform inverse problem by allowing a natural decoupling between

the frequencies of the signal and thus, between the corresponding wavenumbers of the model. Inverting lower-frequency components first strengthens their relative importance if they are not dominant in the spectrum of the signal and helps in providing a kinematically better constrained model to invert higher components. It is possible to follow an analogous strategy in the time domain (Kolb *et al.* 1986), but this requires bandpass filtering of the data.

The first implementation of waveform modelling in the ($\mathbf{r}$, ω) domain (Pratt 1990) confirmed its feasibility and interest. However, the technique was limited by its high numerical cost, particularly concerning the required random access memory. Subsequent developments (Jo *et al.* 1996; Shin & Sohn 1998; Šteckl 1998; Šteckl & Pratt 1998; Min *et al.* 2000) made the approach more attractive by strongly reducing this requirement.

The frequency-domain inverse problem was first implemented through a linear functional analysis (Pratt & Worthington 1990; Song *et al.* 1995; Pratt *et al.* 1996), analogous to that used in the time domain, and then rewritten in an equivalent, but mathematically simpler form, using a matrix formulation (Pratt *et al.* 1998). The results obtained with any of these formalisms, on both synthetic (Pratt & Worthington 1990; Song *et al.* 1995; Pratt *et al.* 1996; Forgues *et al.* 1998) and real data (Song *et al.* 1995; Pratt 1999; Pratt & Shipp 1999; Hicks & Pratt 2001) demonstrated the validity of the frequency-domain inversion approach and confirmed its huge advantages, mentioned above, for both modelling and inverting data.

Compared with more usual traveltime techniques, waveform inversion provides a significant improvement in the resolution of tomographic images (Williamson 1991; Pratt *et al.* 1996; Pratt 1999). The achievable resolution depends on the scattering angles, or equivalently, offsets, but can be reduced down to half of the wavelength of the signal in the case of reflected arrivals (Wu & Toksöz 1987); in contrast, the resolution length in traveltime tomography is approximately the size of the first Fresnel zone (Williamson 1991). In the experimental case we are going to present in this paper, there is approximately an order of magnitude in the respective resolution thresholds of traveltime and waveform tomography. Furthermore, waveform inversion theoretically allows one to invert for any physical parameter featuring in the wave equation (density, attenuation factor, Lamé parameters in the elastic case, etc.), whereas traveltime inversion, which only deals with picked events that are generally *P*-wave arrivals, is only sensitive to the velocity of these waves.

On the other hand, the seismic waveform inverse problem is characterized by: (1) a significantly heavier numerical cost and (2) a much narrower linearity domain compared with those of the traveltime inverse problem. This latter aspect makes the use of a complementary method together with waveform inversion preferable in order to provide a good starting model (from a kinematic point of view) from which the iterative convergence scheme is likely to reach the global minimum of the misfit function; a use of waveform inversion alone yields meaningful results only if such a starting model is available independently (Igel *et al.* 1996; Pratt *et al.* 1996; Forgues *et al.* 1998; Djikpesse & Tarantola 1999). Techniques of traveltime fitting are methods of choice to complement waveform inversion or any high-resolution migration-inversion method. They can be considered through global non-linear approaches, including Monte Carlo (Cary & Chapman 1988), genetic algorithms (Sambridge & Drijkoningen 1992; Sen & Stoffa 1992; Jin & Madariaga 1993) and simulated annealing (Xia *et al.* 1998) techniques for 1-D problems only, or through a local approach, in which the dependence on the initial model is much weaker than for the waveform fitting problem and where such an appropriate model can generally be easily designed (Pratt & Goulty 1991; Zhou *et al.* 1995, 1997; Pratt 1999; Pratt & Shipp 1999). These traveltime preliminary approaches are interesting in that they allow one to build a starting model for which the degree of kinematic agreement with data can be controlled below half a signal time period. This threshold represents the limit above which waveform inversion is likely to converge in a secondary minimum due to phase ambiguity (cycle skip), which is a usual cause of failure.

In our own application, the background has a constant and known velocity but the size and velocity contrast of the scattering objects require a non-uniform initial model for the waveform inversion to succeed, as we shall illustrate. To this end, a linearized traveltime tomography approach, similar to those of Toomey *et al.* (1994) and Zelt & Barton (1998), is adopted, as in the works of Pratt (1999) and Pratt & Shipp (1999).

In this paper, we deal with experimental laboratory data. An ultrasonic tomography experiment was performed at the University of Rennes (France) in a water tank. In this experiment, we aim to:

(1) validate and test the frequency-domain waveform inversion method we are advocating here in a real data processing context,

(2) find a procedure to combine the information brought by various scattering angles, using two different tools, namely waveform inversion and traveltime tomography, to solve a strongly non-linear tomographic problem.

The ultrasonic experiments performed in this tank were initially devoted to the development of an endoscopic borehole seismic method, including works on deconvolution and signal processing (Valéro 1997). This experimental device was also used for developing laboratory-scaled characterization methods for rock samples using ray-Born-based asymptotic waveform inversion (Ribodetti *et al.* 2000; Saracco *et al.* 2000). There are many common features between the data set presented and processed in the study of Ribodetti *et al.* (2000) and our own data set, the acquisition of which is described in the following section. Apart from the fact that different scatterers were used, there are also noticeable differences between these two experiments: (1) we used five different offsets in our own experiment instead of just one; (2) two scatterers were immersed to show the ability of finite-difference-based waveform inversion to deal with multiscattered waves; and (3) we do not invert for the Q attenuation factor, although its effect is taken into account in our modelling of data.

Compared with other laboratory experiments in which waveform inversion or diffraction tomography techniques were used (Pratt & Worthington 1988; Pratt & Goulty 1991; Pratt 1999), we deal with a geometrically simple model, circularly surrounded by the data acquisition geometry. On the other hand, the coverage is limited (five receivers per source) and, above all, we deal with much stronger acoustic velocity contrasts (up to approximately 200 per cent instead of a few per cent to a few tens of per cent) and therefore, find ourselves in an arduous case where the weak scattering linearizing assumption of these methods is clearly not verified. Yet, comparable conditions could possibly be met in certain specific surface applications and it appears worthwhile to assess the solutions that could be proposed for such problems.

A detailed description of the experimental set-up is given in the second part of the paper. The resultant data sets are presented in the third part together with their pre-processing sequence. In the fourth and fifth parts, we present both the modelling and inversion aspects of waveform and traveltime tomography used in our data processing. The final part presents and discusses the results obtained with the tomographic strategy we propose for this problem.

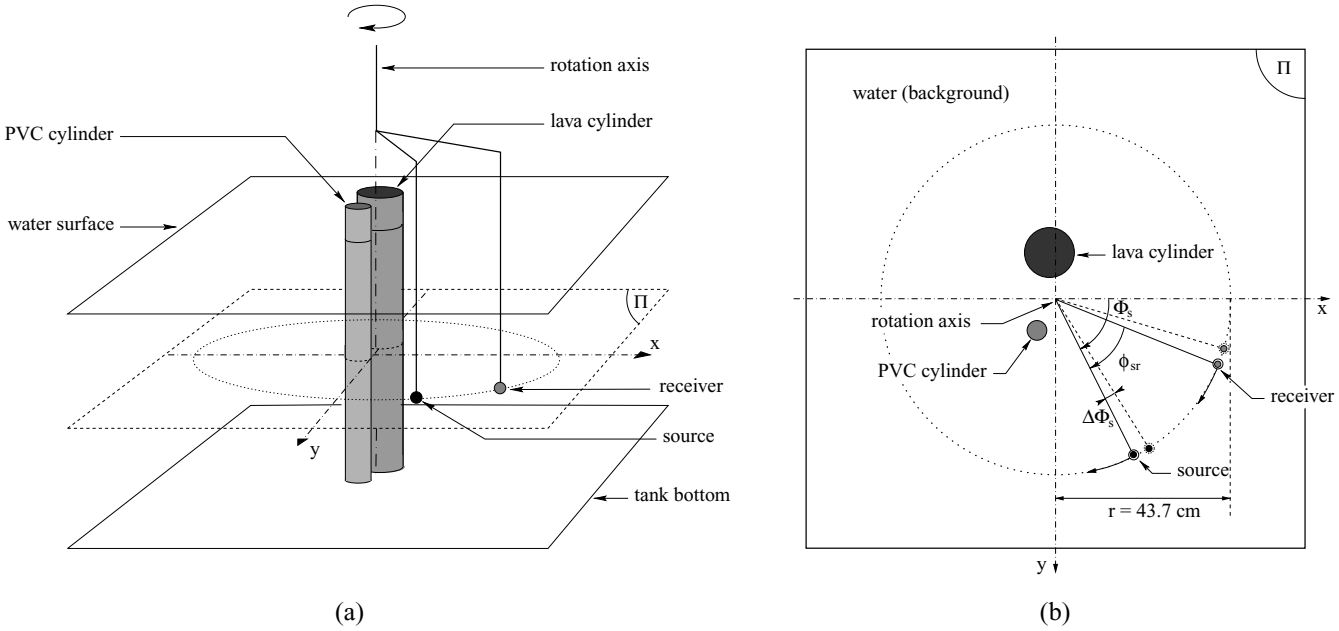

Figure 1. Data acquisition geometry. (a) General view, (b) view in plan Π: Φ_s denotes the angle between the source and its reference position, $\Delta\Phi_s$ is the angular increment between two successive shots and ϕ_{sr} is the angle between the source and the receiver.

2 EXPERIMENTAL SET-UP

The experiment was carried out in a water tank, the dimensions of which are 2.00 × 1.40 × 1.50 m^3 (see Fig. 1). The water temperature was 20 °C and remained constant during the experiment. Tables taken from Greenspan & Tschiegg (1959) give a corresponding *P*-wave velocity of 1482.66 m s^{-1}. This estimation was confirmed by a transmission experiment performed using high-frequency transducers (500 kHz for the dominant frequency), which yielded a value of 1482.64 ± 4.6 m s^{-1}. The corresponding density was considered to be 1000 kg m^{-3}. Two scatterers were immersed in the tank. The first one is a lava cylinder of diameter 11.8 cm, for which the *P*-wave velocity and density are estimated as 4500 m s^{-1} and 2500 kg m^{-3}, respectively. The second scatterer is a PVC cylinder with a diameter of 6.7 cm, a *P*-wave velocity of approximately 2400 m s^{-1} and a corresponding density averaging 2000 kg m^{-3}. Unlike the PVC target used in the study of Ribodetti *et al.* (2000), which was a hollow tube, our two targets are filled cylinders. They thus have a more limited wavenumber bandwidth that should be more exhaustively covered by the signal we use, which is itself band-limited (see below). The two cylinders rest vertically on the bottom of the tank through supports (Fig. 1a). The acquisition geometry consists in a source and a receiver that are bound to a rotation axis. They are immersed at the same depth and rotate together around the axis, describing a circular horizontal loop around the two scatterers. The experimental conditions are comparable with those of medical tomography but we deal here with a 2.5-D problem and not a fully 3-D one. A clockwise angular increment $\Delta\Phi_s$ of 5° with respect to the rotation axis is performed between two successive shot positions, leading to 72 seismic traces for the whole loop (one trace per shot). Five similar experiments were performed with different angles ϕ_{sr} between the source and the receiver (Fig. 1b), the values of which are set to approximately 20°, 60°, 100°, 140° and 180°, respectively (the real values are given in Table 1 but we will refer to these 'rounded' values in the forthcoming developments for simplicity). We thus have a variety of situations between backscattered (reflected) data and forward scattered (transmitted) ones. The angle between the source and the receiver was manually adjusted (leading to the slight differences with respect to the 'rounded' values), whereas the rotation of the source/receiver device between two shots is performed by a computer-controlled rotating engine and is very accurate.

Table 1. Angle ϕ_{sr} between the source and the receiver in the five experiments. The discrepancy comes from experimental conditions.

Theoretical values	20°	60°	100°	140°	180°
Experimental values	20.83°	60.60°	100.86°	141.45°	178.40°

The source and the receiver are two similar piezo-electric hydrophones (Brüel & Kjær type 8103) that can work in forward (source) or reverse (receiver) mode. Their size is slightly less than 1 cm in each space direction and they act as point sources and receivers. The acquisition is controlled by a computer-based device. A signal (second derivative of a Gaussian pulse) is synthesized and electronically amplified before being sent to the source hydrophone. As a result of a slightly non-linear response of the amplifier and mainly, to subsequent interactions between the source and the small plexiglass cube carried by a rod it is fixed to, the signal is strongly distorted and made anisotropic as we shall see. After being propagated in the tank, the resulting wavefield is recorded at the receiver position, linearly re-amplified (without distortion), digitized and stored in an output file.

A time signature of the signal used in the forthcoming processing is displayed in Fig. 2 with its corresponding frequency spectrum; the dominant frequency is approximately 36 kHz. When the wavefield is propagated, it becomes not only scattered by the immersed objects but also by other discontinuities, namely, the tank side walls and bottom and the free boundary at the water surface. The recorded signal is thus polluted by strong coherent events that can be synchronous with the scattered signal of interest. This problem is overcome with a dual acquisition procedure: a second similar acquisition is performed in which the cylindrical scatterers are removed from the tank. The events recorded during this second experiment are the

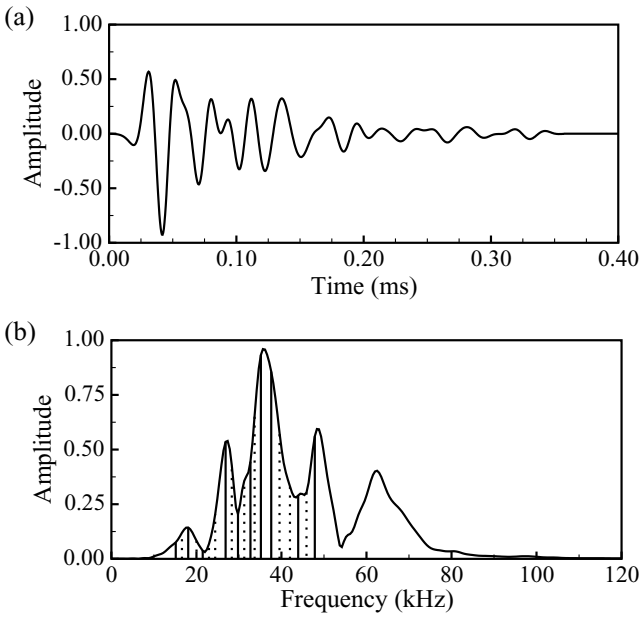

Figure 2. Source wavelet used during the processing (a) and corresponding amplitude spectrum (b). The straight vertical lines in (b) indicate the 10 frequencies used initially in waveform tomography, the dotted ones corresponding to the 10 extra frequencies added further in the processing.

direct wave and the polluting reflections mentioned above. By simply subtracting this second data set from the first one, the reflections are removed, or at least, strongly attenuated and the diffracted signal of interest is enhanced. The same strategy was followed in the work of Ribodetti *et al.* (2000).

3 PRE-PROCESSING OF DATA

The data resulting from our experiment are displayed in Figs 3–5. For the sake of brevity, we will term 'X° data' the data subset corresponding to $\phi_{sr} = X^\circ$. Fig. 3 illustrates the dual experiment method, showing the 20° raw data with and without the scatterers, and the 'cleaned' data obtained by subtraction and a time windowing, applied to remove the remaining unwanted events. The source and receiver positions were almost exactly reproduced between the two acquisitions (note, however, the small remaining artefacts in Fig. 3c); the input signal was itself rigorously reproduced and any renormalization prior to the subtraction was unnecessary.

This technique of dual acquisition and subsequent subtraction remains meaningful as long as the direct and scattered wavefields are distinct in time. A careful examination of data and simple considerations on traveltimes (to obtain an approximate idea of the scatterers positions and dimensions) show that this condition holds for the 20°, 60° and 100° data subsets. For $\phi_{sr} = 140^\circ$ and 180°, the distinction can no longer be made and the pre-processing sequence is different. The direct arrival has to be removed (by time windowing) from the scatterer-free data subset before being subtracted from the other corresponding subset (with scatterers) in order not to alter the recorded scattered wavefield while removing parasitic reflections.

Figs 3(c) and 4 show all the data subsets after these pre-processing operations and a bandpass filtering (according to the source spectral content) have been performed.

Although the different subsets were recorded at different times, the source positions and signal were again accurately repeated here. Hence, for a given source position, the five data subsets can be seen as a recording of the same wavefield at different receiver positions. In particular, the relative amplitudes between offsets are correct and mixing these data together reproduces a virtual multi-offset experiment in which five distinct receivers would have simultaneously recorded the wavefield propagated from one source. This allows one to mix the various subsets during our tomographic processing and possibly, to eventually deal with just one data set.

However, care must be taken in doing so. For a given source, the 140° and 180° data represent a recording of the whole wavefield that would have propagated in an infinite medium as walls and free boundary reflections have been removed. In contrast, the 20°, 60° and 100° data subsets, from which the direct arrival has been removed with unwanted reflections, only correspond to a recording of the scattered part of this wavefield. During waveform inversion, it is possible to remove the effect of the direct wavefield and reproduce this by simply subtracting the corresponding data, computed as a first step in the homogeneous background model, to the data computed in the successive iterates of the model. By doing so, we proceed in a very similar manner to that applied while pre-processing the 20°–100° data subsets. When dealing with the 140° or 180° data, this subtraction is meaningless since no distinct direct arrival exists in these subsets. Hence, a problem arises when one wishes to process any combination of these two kinds of data, respectively, termed reflection and wide-angle data from now on. The natural solution is to process the full-wavefield data by including both the direct and the diffracted arrivals in the reflection data subsets to make the problem physically consistent. A direct arrival has to be re-added on subsets from which it had been previously removed with unwanted reflections. The simplest way to do this would be to isolate the direct arrival (by time windowing) from the data recorded with no scatterer and to add it to the corresponding diffracted data to obtain full-wavefield, artefact-free data. However, this approach is incorrect because of the source directivity. As already mentioned, the signal emitted by the piezo-electric transducer becomes not only distorted but also made strongly anisotropic by the interaction with the source-carrying device. Consequently, the signal radiated towards the scatterers and the direct wavefield have noticeably different signatures, particularly for small values of ϕ_{sr} (Fig. 6). On the other hand, the waveform modelling only generates isotropic wavefields. Considering that only the diffracted part of the wavefield is of interest in our problem, it seems wise to use the time signature of the signal that propagates towards the scatterers for our modelling signal. However, by doing so, we will model a direct wavefield, the signature of which is significantly different from that recorded in the data. Since the direct wavefield carries no information concerning the scatterers but exhibits fairly higher amplitudes than the scattered one, an incorrect modelling of this first energetic arrival will make the inversion process unable to exploit any scattered information and will lead to a failure of waveform inversion. If the direct arrivals are included, they have to be entirely 'explainable' by the starting model and the modelling signal, in order for the search to become immediately and only focused on the diffracted part of the wavefield in spite of its relatively weak amplitude. We fulfilled this requirement by computing time-domain synthetic direct arrivals with the input signal used for the inversion. This is achieved with our frequency-domain finite-difference modelling tool, described in the next section; an inverse Fourier transform brings the result back to the time domain. These synthetic direct wavefield data are subsequently added to the real scattered ones, leading to the three 'hybrid' data sets presented in Fig. 5. A general schematic view of the whole pre-processing phase that summarizes all of these points is given in Fig. 7.

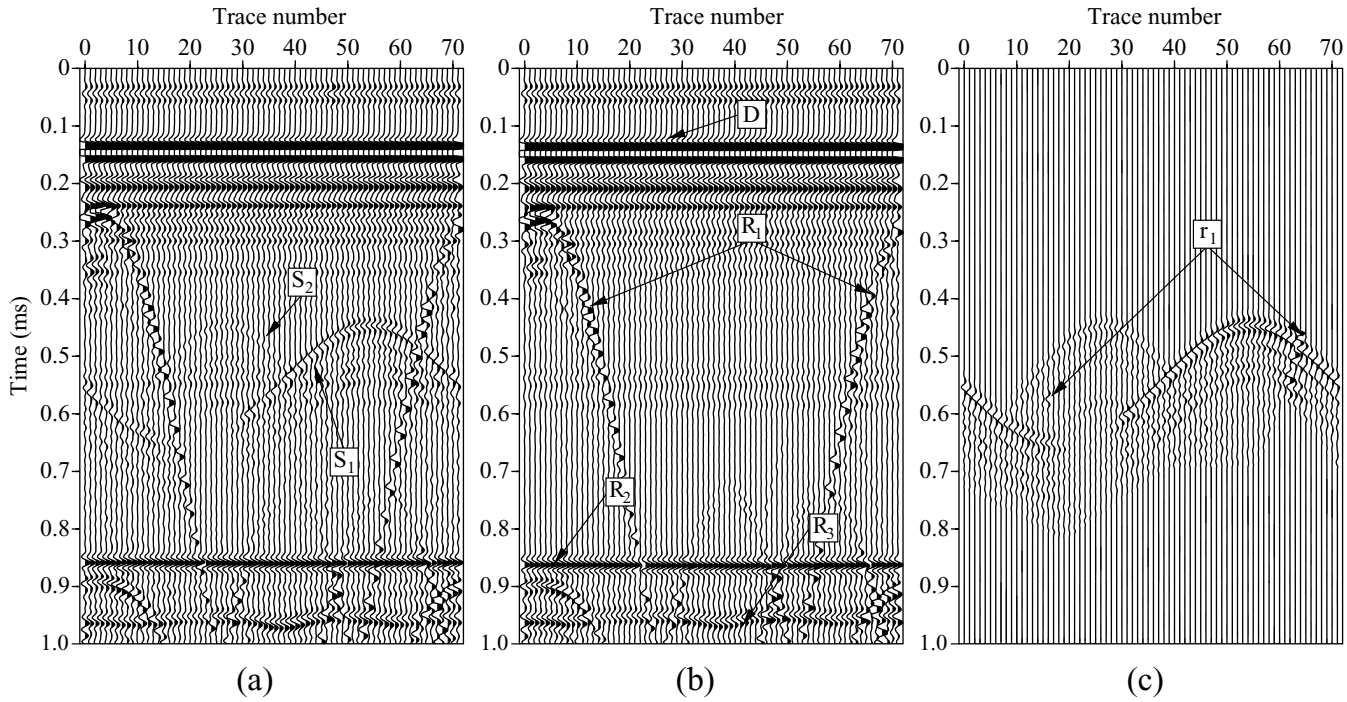

Figure 3. Seismograms obtained for $\phi_{sr} = 20^\circ$ with (a) and without the scatterers (b). S_1 and S_2 denote the scattered arrivals (by the PVC and the lava cylinders, respectively). D denotes the direct arrival, R_1, R_2 and R_3 denote the reflections on one side wall, the free surface and the tank bottom, respectively. Subtracting these data and time windowing the result leads to (c). Label r_1 denotes remaining artefacts due to small positioning discrepancies between the two experiments.

To perform the synthetic direct wavefield modelling, and waveform inversions, a time signature of the source signal had to be designed. As we just mentioned, we considered that the diffracted energy was roughly emitted towards the source/receiver rotation axis close to which the scatterers appear to be located. Hence, the signal of interest could be found in the 180°, scatterer-free data. We simply applied a time window filter on these data to remove polluting reflections, stacked traces to increase the signal-to-noise ratio and time-shifted the outcoming signal according to the travelling distance of the wavefield between the source and the receiver and to the water velocity. This signal and its amplitude spectrum are given in Fig. 2.

Concerning the traveltime inversion we also performed during our processing of data, the modelling tool is an eikonal equation solver (Hole & Zelt 1995) that computes the first-arrival traveltime. During the inversion, the model is updated to fit picked first arrivals as we shall see next. In our problem, this technique is only relevant if the first-arrival time is influenced by the presence of the scatterers or, in other words, if the first arrival is not a direct wave but a forward-scattered one. As we saw, this condition holds only for the 140° and 180° data and this is why traveltime tomography is only applied on these subsets. No further pre-processing was required to pick first arrivals.

4 FREQUENCY-DOMAIN WAVEFORM MODELLING AND INVERSION

4.1 Frequency-domain 2-D visco-acoustic modelling

Our waveform modelling tool is a full wave equation solver. We limit our scope to the scalar wave equation and make the assumption that wave conversions are negligible in our experiment. Fourier transforming the time-domain acoustic wave equation yields the frequency-domain equation:

$$-\frac{\omega^2}{\kappa(\mathbf{r})}p(\mathbf{r},\omega) - \nabla\cdot\left[\frac{1}{\rho(\mathbf{r})}\nabla p(\mathbf{r},\omega)\right] = s(\mathbf{r},\omega), \tag{1}$$

where κ and ρ denote the local values of bulk modulus and density; p denotes the pressure field and s denotes the source term. Including a Q attenuation factor is straightforward in the frequency domain (Song *et al.* 1995; Pratt 1999) and is carried out with a complex-valued κ coefficient (Kjartansson 1979). A 2-D form of eq. (1) is discretized using the nine-point differencing scheme of Jo *et al.* (1996) and recast as an implicit linear system

$$\mathcal{Z}(\omega)\mathbf{p}(\omega) = \mathbf{s}(\omega), \tag{2}$$

in which $\mathbf{p}$ and $\mathbf{s}$ are the vectors formed by collecting the values of p and s at the nodal points of the numerical grid. Up to here, the ordering of these points is unimportant. The square matrix $\mathcal{Z}$ is sparse and gathers the wave equation differencing operators (Pratt 1990). Inverting eq. (2) is numerically very costly and unnecessary since it can be equivalently written as

$$\mathcal{L}\mathcal{U}\mathbf{p} = \mathbf{s}, \tag{3}$$

where $\mathcal{L}$ and $\mathcal{U}$ are lower and upper triangular matrices resulting from the LU factorization of $\mathcal{Z}$ (see, for example, Press *et al.* 1992). As pointed out in previous studies (Marfurt 1984; Pratt 1990), a direct LU resolution of eq. (2) yields considerable benefit for problems involving numerous independent sources. Indeed, once the $\mathcal{L}$ and $\mathcal{U}$ factors are obtained, the solution for any second member is quickly computed by performing the elimination and substitution steps of the LU solving scheme. This is the crucial advantage of a direct method over an iterative one in the context of exploration seismic experiments in which numerous sources are generally involved.

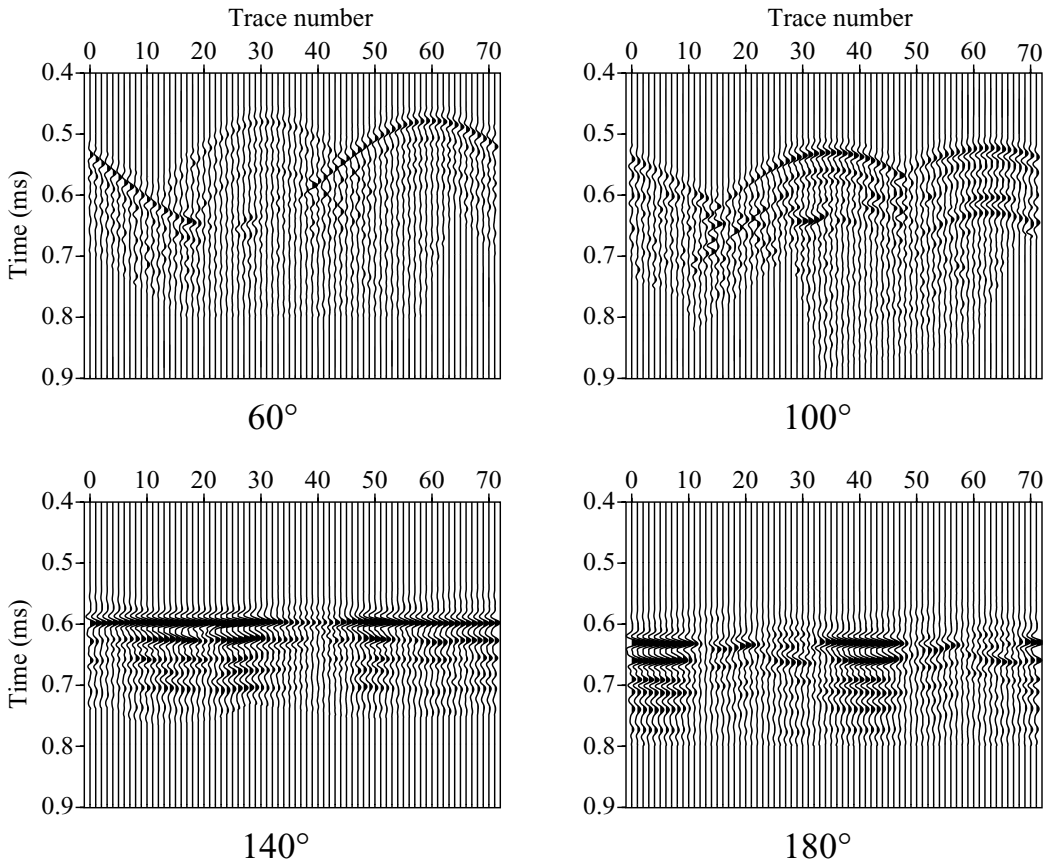

Figure 4. Seismograms obtained for the remaining data subsets after subtraction. 60° and 100° data correspond to the scattered part of wavefields (such as the 20° of Fig. 3c), whereas the 140° and 180° data are full-wavefield recordings.

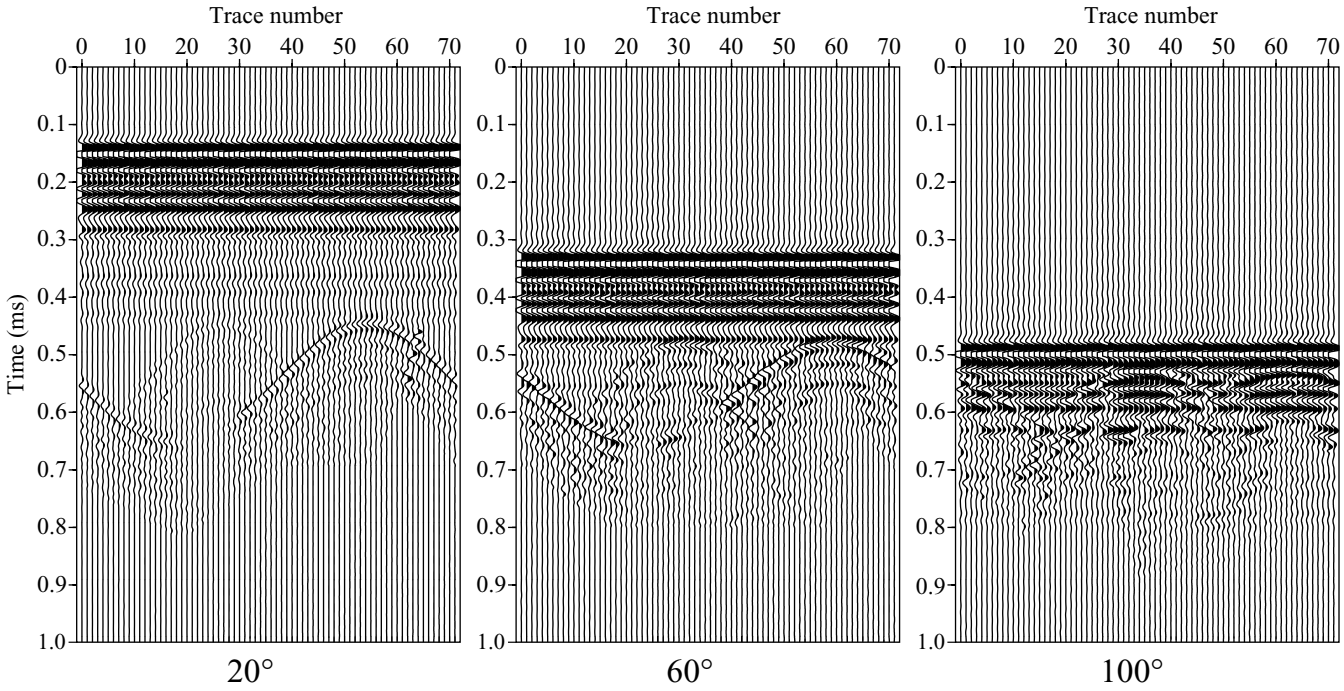

Figure 5. 'Hybrid' seismograms for the 20°, 60° and 100° data after a synthetic direct arrival has been added to overcome the problem of source anisotropy and make the problem physically consistent with respect to wide-angle data.

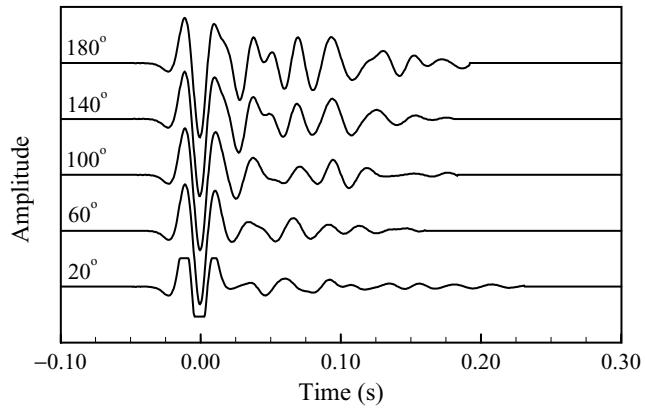

Figure 6. The direct wavefield time signature for each value of ϕ_{sr} illustrates the problem of source anisotropy. Note that the receiver response is saturated at 20° due to its proximity with the source.

However, this aim is reached at the expense of important memory resources, used to store the $\mathcal{L}$ and $\mathcal{U}$ factors, since $\mathcal{Z}$ becomes partially filled during its factorization. This limitation can be partially overcome by the use of an adequate ordering scheme, the filling being dependent on the matrix initial ordering. The nested dissection technique (George & Liu 1981) consists in a specific numbering of the grid nodes that strongly limits the number of non-zero coefficients appearing during the factorization. It was successfully applied to this problem (Šteckl 1998). We adopted a slightly different approach and implemented a highly optimized linear solver (Ma41) from the Harwell Subroutine Library. This software first elaborates and performs a re-ordering of the matrix it is given in input before factorizing it and solving the system for any right-hand side vector. The re-ordering scheme is based on an approximate minimum-degree algorithm (Amestoy *et al.* 1996) and is flexible, since no grid-dependent ordering is preliminarily defined. The memory savings are similar to those offered by a nested dissection algorithm and the computation time drops dramatically compared with a sequential ordering-based resolution of eq. (2). Furthermore, the Ma41 software has a multiple right-hand side option that allows a simultaneous resolution for numerous second members and a speed up of the resolution phase (elimination and substitution steps) at the expense of an extra memory cost.

The frequency-domain wave equation resolution, being a boundary value problem, numerical absorbing conditions at the edges of the modelling grid are of crucial importance. We implemented a Perfectly Matched Layer scheme derived from Collino (1997) that requires only seven points per absorbing layer with a fairly good

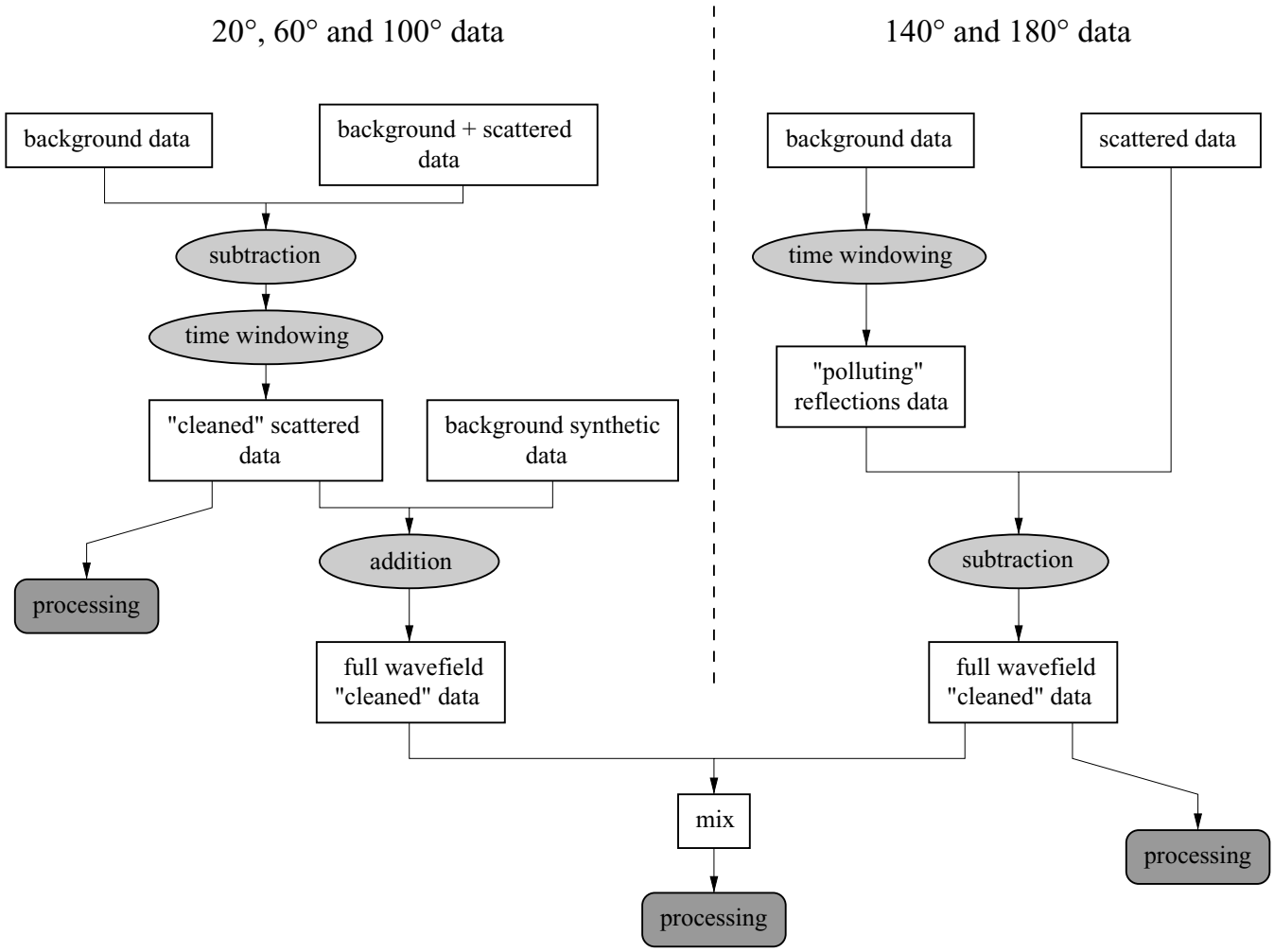

Figure 7. Data pre-processing schedule. The sequence depends on whether a direct arrival can be separated from the rest of the recording ($\phi_{sr} = 20°, 60°, 100°$) or not ($\phi_{sr} = 140°, 180°$).

attenuation of the reflected echos, essentially independent of the wave frequency and direction of propagation.

4.2 Frequency-domain waveform inverse problem

Considering the computational cost of the modelling, any global approach of the strongly non-linear seismic waveform inverse problem is out of reach. Instead, a local iterative approach is adopted in which one seeks to converge towards the true model by minimizing a function σ that quantifies the misfit between the experimental data and those computed in the successive iterates of the model. A model corresponds to a point in the model parametrization space. A gradient of the misfit function is calculated at this point. Subsequently, a step that ensures a decrease of the misfit is performed in the indicated descent direction, resulting in a new model that yields a better data fitting. The operation is repeated until some convergence criterion is fulfilled, the final model theoretically corresponding to the minimum of σ and thus, to the searched model. The non-linearity of the inverse problem results in a non-quadratic misfit function (in the usual case of a least-squares formulation) and therefore, local minima are likely to be encountered during the search leading to incorrect models that seem to minimize σ. To avoid such mistakes, the search has to be initiated from the region of the assumed global minimum of the function. This mathematical condition has a physical expression in terms of model wavelengths: the starting model has to contain the smooth variations of the model, the wavenumbers of which are below those covered by the investigating signal (see, for example, Mora 1987; Pratt *et al.* 1996; Forgues *et al.* 1998). In other words, only wavelengths that yield scatterings of the incident wavefield can be retrieved through waveform inversion.

In the forthcoming theoretical developments of the iterative converging scheme, we briefly summarize the matrix formalism of Pratt *et al.* (1998). Let first consider an observed data set

$$\mathbf{d}^{(\mathrm{obs})} = \left[d_i^{(\mathrm{obs})}\right], \quad i \in [1, n_d], \tag{4}$$

where n_d represents the number of source/receiver pairs (data space dimension). Let also consider a computed data set $\mathbf{d}(\mathbf{m})$, corresponding to a model parameter set $\mathbf{m}$ of the n_m-dimensional model space. A residual vector can be expressed as

$$\delta\mathbf{d}(\mathbf{m}) = \mathbf{d}(\mathbf{m}) - \mathbf{d}^{(\mathrm{obs})}. \tag{5}$$

Using an l_2 norm, the misfit function is defined by

$$\sigma(\mathbf{m}) = \frac{1}{2}(\delta\mathbf{d}^{\mathrm{t}})^{*}\delta\mathbf{d} \tag{6}$$

with the usual notation t and * representing the vector or matrix transpose and complex conjugate, respectively.

The σ function gradient at the current point $\mathbf{m}$ in the model space is given by

$$\nabla_{\mathbf{m}}\sigma(\mathbf{m}) = \frac{\partial\sigma}{\partial\mathbf{m}}(\mathbf{m}) = \mathcal{R}e[(\mathcal{F}^{\mathrm{t}})^{*}\delta\mathbf{d}], \tag{7}$$

where $\mathcal{R}e$ denotes the real part of the complex-valued bracketed expression and $\mathcal{F}$ is the Fréchet operator, mapping the model space to the data space, for which the kernel is given by the $(n_d \times n_m)$ matrix

$$\mathcal{F}_{i,j} = \frac{\partial d_i}{\partial m_j}. \tag{8}$$

Introducing the virtual source term matrix $\mathcal{V}$ (see Pratt *et al.* 1998, for details), with columns given by

$$\mathbf{v}^{(j)} = -\frac{\partial\mathcal{Z}}{\partial m_j}\mathbf{p} \tag{9}$$

and expressing $\mathcal{F}$ with $\mathcal{V}$ and the impedance matrix $\mathcal{Z}$ of the wave equation, we obtain the final expression of the gradient vector

$$\nabla_{\mathbf{m}}\sigma(\mathbf{m}) = \mathcal{R}e[\mathcal{V}^{\mathrm{t}}(\mathcal{Z}^{-1})^{\mathrm{t}}\delta\widetilde{\mathbf{d}}^{*}], \tag{10}$$

where $\delta\widetilde{\mathbf{d}}$ is a vector obtained by mapping $\delta\mathbf{d}$ at the receiver positions in the n_m-dimensional modelling grid and setting the $n_m - n_d$ remaining coefficients to zero. Note that for simplicity in vector and matrix manipulation, forward and inverse problems are assumed to be solved on the same grid, which is not mandatory (Pratt *et al.* 1998; Hicks & Pratt 2001). A component j of the gradient vector can be expressed as

$$(\nabla_{\mathbf{m}}\sigma)_j(\mathbf{m}) = \mathcal{R}e\left[\mathbf{p}^{\mathrm{t}}\left(\frac{\partial\mathcal{Z}^{\mathrm{t}}}{\partial m_j}\right)(\mathcal{Z}^{-1})^{\mathrm{t}}\delta\widetilde{\mathbf{d}}^{*}\right]. \tag{11}$$

From eq. (11), we have the classical physical interpretation of the gradient which, much as for a migration operator (Lailly 1984; Tarantola 1984), correlates an incident wavefield $\mathbf{p}$, shot from a source, to a back-propagated wavefield $(\mathcal{Z}^{-1})^{\mathrm{t}}\delta\widetilde{\mathbf{d}}^{*}$ shot from a receiver position, with the corresponding source/receiver data residual acting as the source term. The summation over every source/receiver pair is implicit in eqs (10) and (11).

The numerical implementation of eq. (11) requires the computation of:

(1) the incident wavefields $\mathbf{p}$ propagated from every source;
(2) the residual wavefields $(\mathcal{Z}^{-1})^{\mathrm{t}}\delta\widetilde{\mathbf{d}}^{*}$ back-propagated from the corresponding receivers; and
(3) the partial derivative $(n_m \times n_m)$ matrix $\partial\mathcal{Z}^{\mathrm{t}}/\partial m_j$; it has indeed only up to five non-zero coefficients, considering that, regarding the inverse problem, the nine-point scheme (Jo *et al.* 1996), which is relevant for the modelling, is physically equivalent and more expensive from a computational point of view than the basic five-point scheme.

Once the gradient computed, the model is accordingly updated, using the relation

$$\mathbf{m}_{k+1} = \mathbf{m}_k - \alpha_k\nabla_{\mathbf{m}}\sigma(\mathbf{m}_k), \tag{12}$$

where k is an iteration index and α represents the length of the step performed along the steepest descent direction. α can be found by a line search technique that usually requires two to three forward problem computations. A conjugate gradient method can be adopted to speed up convergence (Mora 1987; Tarantola 1987) at negligible extra cost. It is also possible to enhance the gradient components according to their distance with the source and receiver positions in order to compensate for the amplitude loss by geometrical spreading. This operation, usually termed 'gradient pre-conditioning', appears to be very worthwhile in surface seismic applications (due to the low-amplitude coverage at the bottom of models). It appeared to be of smaller benefit, though not completely useless, with the circular coverage we have in the experiment presented in this paper.

5 FIRST-ARRIVAL TRAVELTIME TOMOGRAPHY

As for waveform inversion, the traveltime tomography tool used in our data processing seeks to iteratively minimize the misfit between observed and computed data, starting from an initial model. The main difference comes from the noticeably wider linearity domain of time tomography that makes conditions on the initial model much less restrictive than those of waveform tomography.

The observed data consist in picked first-arrival traveltimes. An iteration of the data fitting procedure decomposes as follows:

(1) first-arrival traveltime tables are computed for each source, in the whole model, by solving the eikonal equation through a finite-difference scheme (Hole & Zelt 1995); this is achieved with the FAST package eikonal solver (Zelt & Barton 1998);

(2) ray paths linking each source/receiver pair are calculated by reverse propagation from the receiver to the source, along the traveltime gradient direction;

(3) the Fréchet derivative matrix $\mathcal{F}_{ij} = \partial t_i / \partial m_j$ assessing the effect of the jth model parameter perturbation on the traveltime between the ith source/receiver pair is calculated;

(4) the following system is solved:

$$\begin{pmatrix} \mathcal{C}_d^{-1/2} \Delta \mathbf{t}^{(k)} \\ 0 \\ 0 \\ 0 \end{pmatrix} = \begin{pmatrix} \mathcal{C}_d^{-1/2} \mathcal{F} \\ \lambda_h \mathcal{S}_h \\ \lambda_v \mathcal{S}_v \\ \epsilon \mathcal{D} \end{pmatrix} \left(\Delta \mathbf{m}^{(k)} \right), \tag{13}$$

in which $\mathcal{S}_h$ and $\mathcal{S}_v$ are horizontal and vertical Gaussian smoothing matrices, respectively, $\mathcal{D}$ is a damping matrix and $\mathcal{C}_d$ is the covariance matrix of data uncertainties; λ_h, λ_v and ϵ are scalars that control the balance between these imposed constraints; the system is solved iteratively using a LSQR algorithm (Toomey *et al.* 1994; Zelt & Barton 1998).

The inversion is non-linear in that ray paths are recalculated for each iteration.

6 DATA PROCESSING

In all of our applications, we consider the initial state of information to reduce to the knowledge of the background properties. This means that the starting models used in our tomographic inversions are either this background model or models obtained by one or several previous traveltime and/or waveform inversion(s) of data.

The approximate knowledge we have of the properties of the scatterers and the positions in the tank allows one to build an image of the model to be retrieved (Fig. 8a). From this, we can assess the wavenumber spectra of both scatterers (Fig. 8b) and also the wavenumber coverage of our waveform tomographic reconstruction with respect to the acquisition geometry (Fig. 9). For each cylinder, this coverage spectrum was obtained by considering every possible diffraction angle in the scatterer for every source/receiver pair and for every inverted frequency. An assumption of single scattering was necessary to compute these coverage diagrams (Devaney 1984; Wu & Toksöz 1987), though multiple scattering is likely to happen here. However, we consider them to provide a reliable estimate of what can be expected from our experiment in terms of reconstruction.

During waveform inversion, a fixed Q factor of 2.1×10^5 (Ribodetti *et al.* 2000), corresponding to water attenuation properties, was included in our modelling. Density was not explicitly inverted either but was derived from the reconstructed velocities using an experimental P-wave velocity/density correspondence curve taken from Ludwig *et al.* (1970).

We also systematically applied a tapered spatial filter on model updates for both tomographic techniques to prevent any reconstruction artefacts (such as Gibbs oscillations for frequency-domain waveform inversion) to appear in regions in which data clearly indicate that the scatterers are not located. Considering the 20° data, simple geometric considerations and the knowledge of water velocity show that both cylinders are located in a circular pattern the centre of which is the source/receiver rotation axis and with radius 15 cm; this is the limit out to which the model remained unchanged during the processing. This condition appeared to be necessary for the traveltime tomography to succeed; it simply brought an improvement on waveform tomography images quality.

The finite-difference waveform modelling steps were performed in a square grid, the side of which is 90 cm long. The grid step was 4 mm along the two Cartesian axis, leading to a 240×240 numerical grid (including seven extra points on the four edges for the absorbing boundaries) and to impedance matrices $\mathcal{Z}$ of order 57 600. The average time and memory required to perform a forward modelling on a Sun Ultra 10 440 MHz workstation were approximately 30–36 s and 91–114 Mb, respectively (depending on the frequency value), roughly divided as follows:

(1) 0.5–0.6 s for the matrix analysis (re-ordering scheme elaboration);

(2) 7–11 s to factorize the matrix, requiring storage of between 58 and 68 Mb of RAM;

(3) 21–24 s and 33 Mb to solve for the 72 source positions (with use of the multiple right-hand side option).

The minimum spatial sampling encountered was approximately 7.75 points per wavelength, which is significantly more than the

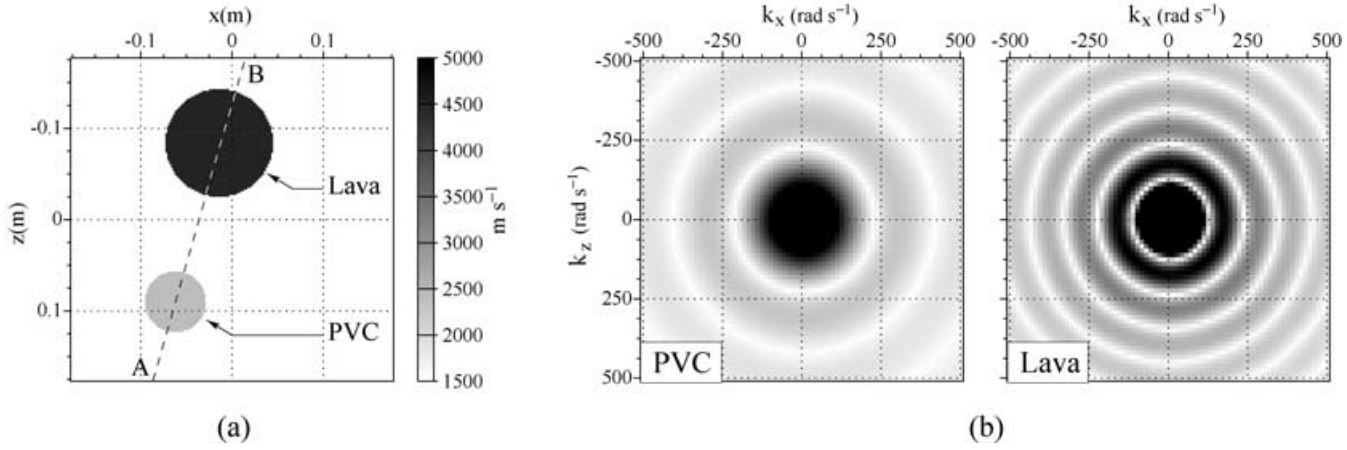

Figure 8. (a) Approximate model for the experiment. [AB] denotes the section through which velocity profiles are displayed for comparisons. (b) Wavenumber amplitude spectra for the PVC and lava cylinder, respectively.

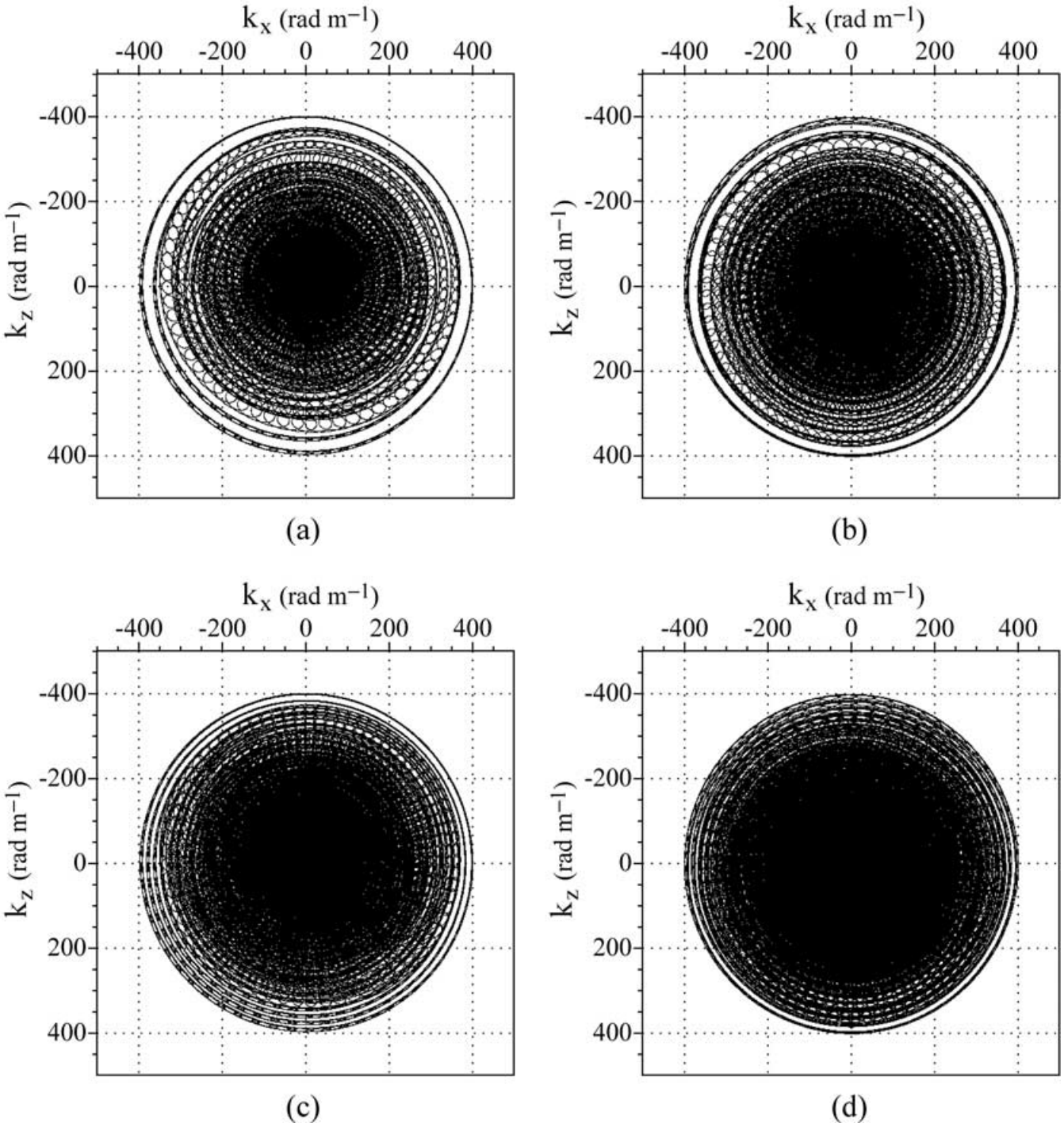

Figure 9. Spectral domain coverage for the complete acquisition geometry. Coverage of the PVC cylinder (a) and the lava cylinder (b) with the 10 frequency waveform imaging. Parts (c) and (d) display the same coverage patterns when the 20 frequencies are used (see Table 2 for the inversion frequency schedule).

Table 2. Signal frequencies used during waveform inversion. The 20 components were used in the combined tomography experiment, whereas only 10 of them (marked by an asterisk) were inverted when only waveform tomography was applied.

Component number	1	2	3	4	5	6	7	8	9	10
Frequency (kHz)	15.14*	16.6	18.07*	20.02	21.48*	22.95	24.41	26.86*	28.32	29.79*
Component number	11	12	13	14	15	16	17	18	19	20
Frequency (kHz)	31.25	32.71*	33.69	35.16*	37.60*	39.55	41.99	43.95*	45.90	47.85*

4.5 gridpoints that represent the threshold above which numerical dispersion errors remain below 1 per cent (Jo *et al.* 1996). Indeed, the limitation of the grid step was usually not imposed by the frequencies to propagate but rather by the requirement to set sources and receivers on node points for the modelling. The source and receiver experimental positions stand on a circular loop and generally do not correspond exactly to a Cartesian modelling grid node position. Hence, they had to be displaced from their theoretical position to the closest node position, resulting in small positioning errors and in potential phase misfits. A 4 mm grid step appeared to limit them below $\sim\lambda/5$ (where λ is the wavelength of the signal) for the higher frequency in Table 2. Equivalent results obtained on more finely discretized models did not exhibit significant improvements but yielded a strong and pointless extra numerical cost. The effect of these positioning errors can be seen on the synthetic direct arrivals that were superimposed on the diffracted data (Fig. 5); small time offsets are visible between neighbouring traces, in contrast with the recorded direct arrivals (label D in Fig. 3b) that are all synchronous. Hicks (2002) proposed a solution to overcome this problem of source positioning in Cartesian grids.

During waveform tomography, the frequencies of Table 2 (or 10 of them for some specified cases) were sequentially inverted, one by one, in increasing order. The converging scheme systematically consisted in a pre-conditioned conjugate gradient algorithm. The convergence criteria were: (1) either a drop of the misfit function below 1 per cent of its initial value or (2) a drop of less than 1 per cent of this function between two successive iterations and in any case (3), the number of iterations was limited to eight (per frequency). Practically, the third condition was frequently encountered first.

Concerning traveltime inversion, the modelling grid dimensions were 451 × 451 with a 2 mm grid step. The CPU time for one iteration was approximately 50 s on a 700 MHz PC running Linux. Five iterations per smoothing level were performed as we shall explain in greater detail in the combined tomography section.

6.1 Results obtained with waveform tomography

The first approach adopted for this tomographic experiment was to only apply our frequency-domain waveform inversion scheme to the data. This can be justified if one considers that the model is supposed to be unknown (except for its background) and that the degree of non-linearity cannot be assessed *a priori*. We defined a set of 10 frequencies, given in Table 2, for which we inverted data.

In frequency-domain waveform tomography, the usual way to recover the features of a model is to reconstruct wavenumbers in an increasing order (Forgues *et al.* 1998). This can theoretically be achieved by either sequentially inverting increasing frequencies of the signal or sequentially inverting data of decreasing offsets, in agreement with the dependence of wavenumber coverage with respect to model illumination (Devaney 1984; Wu & Toksöz 1987). The second approach completely failed from the very beginning and any attempt to invert 140° and 180° data, alone or in combination, starting with the lowest available signal frequency, did not yield any satisfactory result. The problem appears to be very non-linear, as expected, and the homogeneous starting model is too far away from the true model to prevent convergence in secondary minima from occurring. Therefore, the first strategy of inverting every offset with increasing frequencies seemed to be the only possible way in this problem. However, this approach also failed and the non-linearity brought by wide-angle data once again led to secondary minima with none or very few of the features of the model explained. To prevent this, we then only inverted reflection data (the three first data subsets) and this allowed the migration-like reconstruction displayed in Fig. 10(a). The shape of the cylinders is clearly visible but they are surrounded by inversion artefacts (Gibbs oscillations), due to weak coverage. For the same reason, and more particularly the lack of wide-angle data, the lower wavenumbers were not covered and thus, not reconstructed. Now using this model as the initial one (instead of the background), we inverted the whole data set and the result (Fig. 10b) was fairly improved. In particular, the amplitude ratio between the image of the scatterers and the surrounding artefacts was strongly increased. Reiterating the process with two successive inversions of reflection data first, and the complete data set afterwards, starting from this model, led to a further enhancement of the reconstructed image (Fig. 10c). Except for one strong artefact close to the centre of the model, the two cylinders are quite identifiable. The smaller one is partially filled, whereas the larger one remains hollow. The lower wavenumbers could not be reconstructed, even using wide-angle data in our offset combination, and consequently, the reconstructed velocities are far from the estimated velocities for both cylinders. Any further inversion attempt we made, taking this model as the initial one, did not bring any improvement, whatever the offset combination used. Adding other frequency components in the inversion did not change the results significantly either.

These first results show that the problem is too non-linear to be solved by waveform inversion with the homogeneous model as a

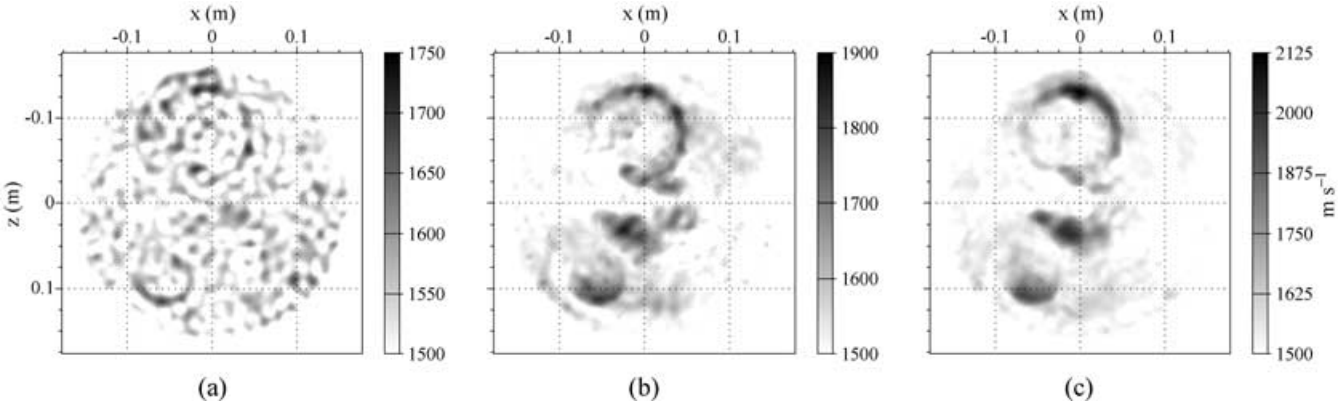

Figure 10. Waveform inversion results. The model in (a) was obtained by combining 20°, 60° and 100° data only, starting from the background model. It was then taken as a starting model to invert the whole data set, yielding the model in (b). The same sequence was repeated once again and led to the model displayed in (c).

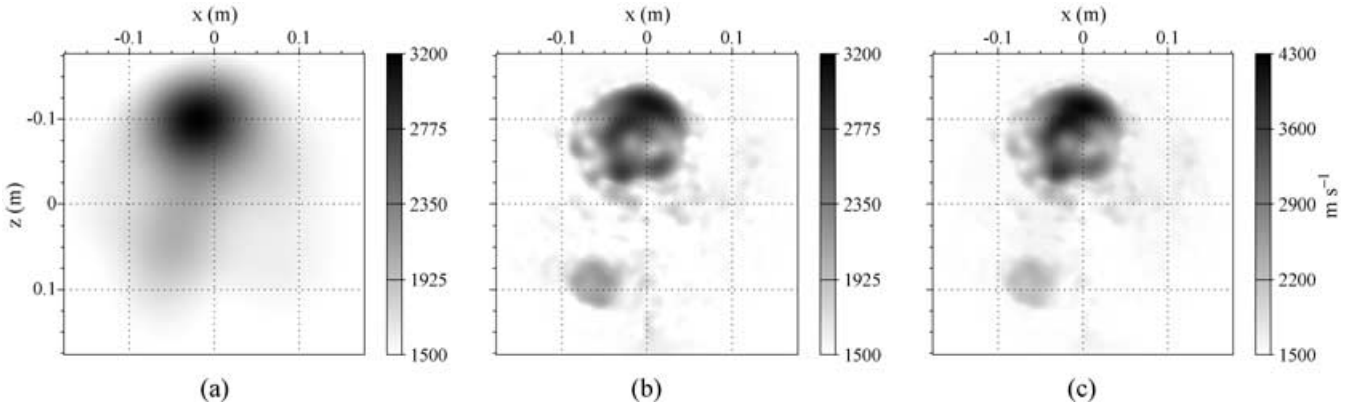

Figure 11. Combined traveltime and waveform inversion results. Traveltime tomography applied in the homogeneous starting model yields the model in (a) from which the model in (b) is obtained using waveform tomography. A further traveltime inversion leads to the model in (c).

starting point. They also show that non-linearity can be partially overcome by first inverting the reflection data and by varying offset combinations but the lower wavenumbers, which are theoretically covered by our acquisition (Fig. 9), could never be recovered.

From this conclusion, we considered that a first approach of the problem with the traveltime inversion tool described above was necessary. This technique can only be applied to the 140° and 180° subsets, as we mentioned. These data are precisely those for which the limitations of the background model as a starting point for waveform inversion appeared to be the most obvious. After the first-arrival traveltimes have been picked on the 180° data, we computed those of the model in Fig. 10(c) for comparison (the eikonal solver of our traveltime tomography tool was used for this purpose). The standard rms misfit between arrival times was found to be 3.66×10^{-2} ms, with a maximum value of 4.85×10^{-2} ms. These values are larger than half a time period of the signal for its lowest inverted frequency ($\approx 3.3 \times 10^{-2}$ ms). We therefore appear to have encountered a case of cycle skip where the phase shift between the signal propagated in our model and the inverted signal is exceeding the limit above which the correlation is likely to be made on incorrect cycle numbers, which is a major cause of non-linearity. This diagnosis, only based on data examination and modelling, is confirmed by calculating the phase-shift introduced by the main scatterer (lava cylinder), using its dimension and estimated *P*-wave velocity. The conclusion is entirely consistent with the conditions expressed by Slaney *et al.* (1984) for reconstructing cylindrical objects using Born-approximation-based diffraction tomography.

6.2 Results obtained with combined traveltime and waveform tomography

Traveltime tomography was applied on the wide-angle data, starting from the homogeneous model. It actually turned out that the inversion could converge towards several models, with essentially the same data fitting, depending on the conditions under which it was carried out. This is, once again, probably a consequence of the poor angular coverage since only two data subsets were available for inversion. In particular, applying the filtering mask (the properties of which were given above) was a critical point in that it prevented large areas of limited velocity contrast with respect to the background from being found.

As for waveform inversion, the quality of results was found to be dependent on how the input information was combined. The best strategy appeared to be an inversion of the 180° data first, from the result of which the 140° data were inverted; finally, the two subsets were merged in a third inversion step. For each of these combinations, five iterations were carried out for three different decreasing smoothing levels, resulting in 15 iterations. The width of the Gaussian smoothing operator was successively set to 50, 20 and 10 mm in both directions, none of them being privileged with respect to the other by the acquisition geometry. Applying this gradually decreasing smoothing helps in reaching a good agreement with data while preventing rays from being trapped in high-velocity spots, hence ensuring a homogeneous spatial coverage of the model. Furthermore, these spots are potentially misleading since their extent is often below the resolution threshold of traveltime tomography.

The result thus obtained can be seen in Fig. 11(a). It is clear that a smoothed image of the cylinders was obtained and we can expect the searched low wavenumbers to be retrieved. A velocity profile of this model along the segment [AB] of Fig. 8(a) is displayed in Fig. 12: velocities were recovered up to 3200 m s^{-1} for the lava cylinder, which is less than the actual estimated velocity (4500 m s^{-1}) given the fact that the lack of spatial resolution of traveltime tomography yields a spread velocity anomaly with smaller amplitude, which fits the data as well. During the inversion, the rms error on traveltimes dropped from 5.41×10^{-2} to 1.81×10^{-3} ms (with maximum values of 7.01×10^{-2} and 3.75×10^{-3} ms, respectively) for the 180° data and from 3.30×10^{-2} ms to also 1.81×10^{-3} ms for the 140° data (maximum values are 4.94×10^{-2} and 3.93×10^{-3} ms). Starting from this model, the waveform fitting inverse problem should therefore be much more linear and in any case, not affected by any problem of cycle skip.

In spite of this important progress, the application of waveform tomography to these data remains difficult. The result obtained with the complete data set, applying the same conditions as when the initial model was the background, yielded an improvement but were still not quite satisfactory. Further conditions were therefore applied and as in our traveltime tomography application, we defined smoothing conditions that were applied to the updating gradient and progressively relaxed. We also added 10 extra frequencies to our inversion schedule (see Table 2) in order to increase the spatial spectral coverage, particularly regarding higher recoverable wavenumbers (Figs 9c and d). With these two new features, we expect to reduce spatial periodicities introduced by discontinuous spectral coverage; the occurrence of these Gibbs oscillations is limited by including new frequencies and their effect is attenuated by smoothing the gradient.

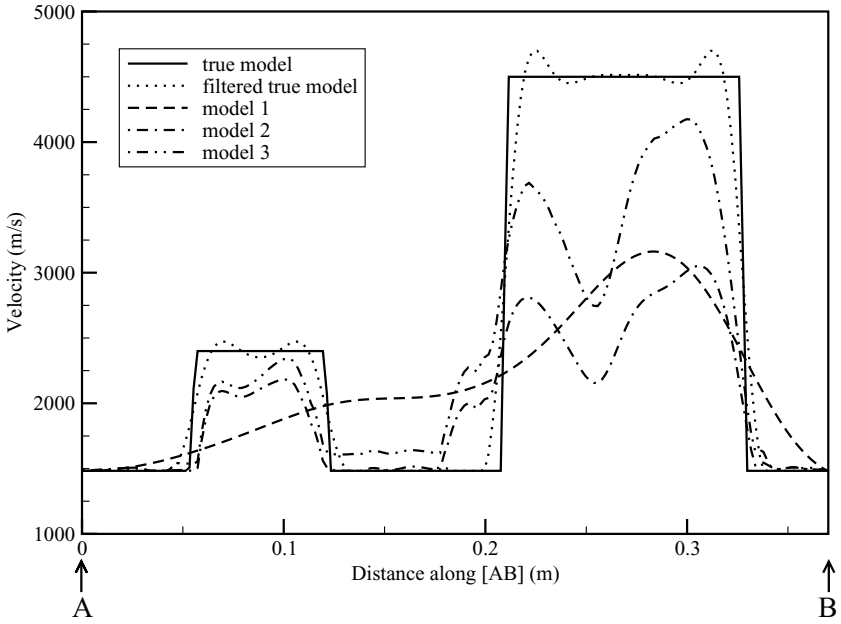

Figure 12. Velocity profiles through the [AB] section of Fig. 8. The solid line is now an estimate of the true model, the dotted line is a filtered version of this model according to the inverted signal spectral coverage. Model 1 is the result of traveltime tomography initiated from the background model, model 2 was obtained by waveform tomography, starting from model 1; a further application of traveltime tomography yields model 3.

We inverted the data with three smoothing levels, here again. For each level, the 20 frequency components were classically inverted by increasing order. The smoothing is performed with a Gaussian operator, the width of which is locally adapted to the wavelength of the signal. The cut-off wavelength is defined as a fraction of the time period of the signal, which was sequentially set to $1/3$, $1/5$ and $1/10$ in the present case.

The result of this waveform tomography strategy can be seen in Fig. 11(b). The resolution was substantially improved and the shape of both cylinders is now quite visible, as in Figs 10(b) and (c). They can be clearly distinguished, which was not the case with traveltime tomography only. The corresponding velocity profile in Fig. 12 confirms that the edges of the scatterers were strongly sharpened. The velocity in the small PVC cylinder was retrieved up to 2100 m s^{-1}. Concerning the lava cylinder, the reconstructed velocities are close to those of the starting model of Fig. 11(a) in spite of the anomaly narrowing. It can also be observed that the cylinder was slightly 'emptied' and features higher velocities on its edges than inside.

Applying traveltime modelling in the model of Fig. 11(b) confirms that the kinematic misfit was re-increased during the waveform inversion step and that the sharpening of velocity anomalies was not balanced by a rise in their reconstructed velocities, at least concerning the lava cylinder. The rms errors were found to be 1.08×10^{-2} and 1.43×10^{-2} ms for the 140° and 180° data, respectively (with maximum values of 1.90×10^{-2} and 1.92×10^{-2} ms). Here again, wide-angle data, which should have provided the balance, appear to have been affected by an intrinsic non-linearity and thus prevented an equivalent degree of kinematic agreement between the waveform tomography input and output models. It is also clear that this remaining non-linearity is not related to any problem of cycle skip. Possible reasons for this will be discussed in a later paragraph. Nevertheless, it is quite clear from Figs 10(c) and 11(b) that the non-linearity of the waveform problem was strongly attenuated, though not completely overcome, by the traveltime preliminary approach.

To try to improve our tomographic model further, we re-applied a traveltime inversion to the model of Fig. 11(b). Usually, traveltime inversion is only applied as a preliminary step to waveform inversion (Pratt 1999; Pratt & Shipp 1999) but the strong non-linearity of our tomographic problem and the kinematic degradation we saw happening during waveform inversion prompted us to try and proceed iteratively with both techniques. We considered that traveltime tomography would enhance the velocity contrast between the scatterers and the background while leaving the image essentially the same in term of focusing, since the high-velocity areas that act as ray traps are physically meaningful here. This hypothesis happened to be verified provided that the width of the smoothing operator used during the inversion was kept reasonably small. Five iterations were performed with combined 140° and 180° data, with a 20 mm wide smoother and resulted in the model displayed in Fig. 11(c). The rms error was brought back to 9.07×10^{-4} ms with a maximum error of 4.13×10^{-3} ms. The velocity in the lava cylinder was increased up to 4200 m s^{-1}, which we consider to be in good agreement with the estimated 4500 m s^{-1}. The small lower velocity zone close to the cylinder axis was not corrected. It could have a physical meaning, since the lava cylinder is probably not homogeneous, but we consider it much more likely to see it as a waveform inversion artefact that was not removed during the following traveltime inversion. Moreover, nothing in the data suggests the existence of such a feature. The PVC cylinder, which is undoubtedly homogeneous, was reconstructed in almost the best possible manner, considering the finite bandwidth of the reconstructing signal (see Fig. 12).

To assess the validity of the final model, we computed a whole set of synthetic seismograms that can be compared with the real ones (Fig. 13). The fit appears to be satisfactory and the main features in data are explained by our model. However, some differences appear, particularly in the 20° and 60° data for which the amplitude of reflected signals is weaker in our synthetic data. We consider this to be a possible consequence of the wider range of frequencies used during modelling with respect to actually inverted components (Fig. 2); therefore, some high wavenumbers, to which the modelling signal is sensitive, are not present in our model. This explanation is all the more likely since the mismatch is observed on reflection

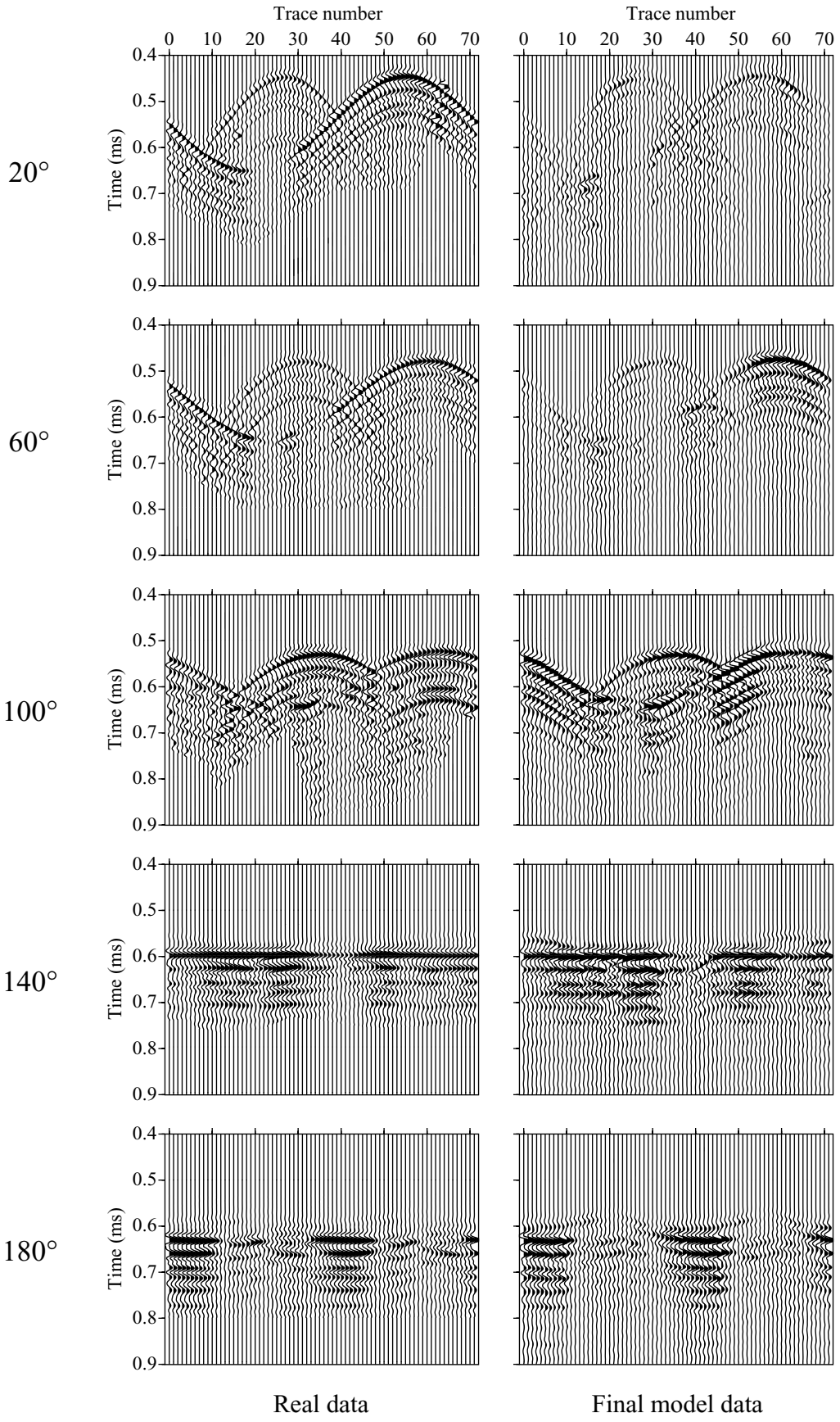

Figure 13. Time seismograms featuring the whole data sets. Real data are shown in the left-hand panel and data computed in our final tomographic model are shown in the right-hand panel.

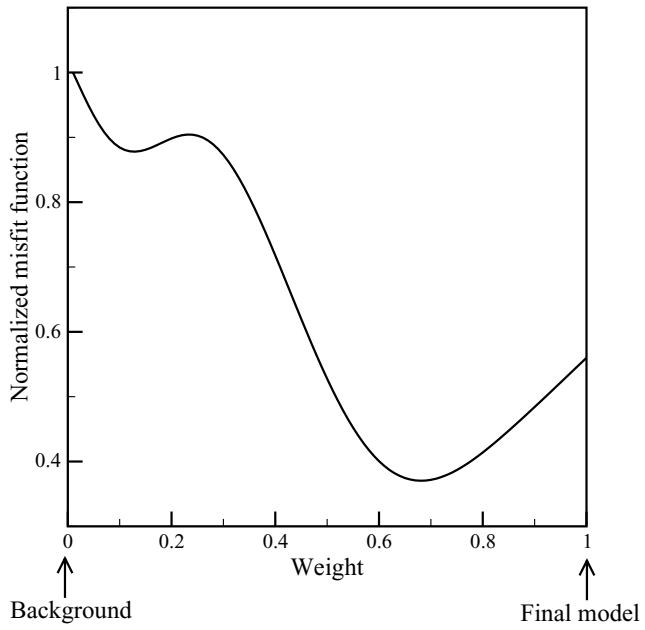

Figure 14. Evolution of the waveform misfit function between the initial and final tomographic models. The abscissa denotes the weight of the final model in the linear combinations used to build the family of hybrid models.

data, which are known to be more sensitive to high wavenumbers than wide-angle ones. Sharper edges in our image of both scatterers would most probably yield enhanced reflected phases.

In the 180° data, differences between synthetic and real data can also be observed, particularly in the two ranges of trace where low-amplitude signals are recorded (roughly from trace 12 to 32 and 48 to 68). These areas correspond to a configuration of acquisition in which the signal is transmitted through both scatterers and possible modelling errors occurring in that situation could explain the locally poor agreement. This point is discussed below.

The non-linearity of our tomographic reconstruction can be illustrated by computing the waveform misfit function in a family of models built by linear combinations of the initial background with the final model, with varying and complementary weights (between 0 and 1). Doing so, we assess the behaviour of the function along a path of the model space between these two extreme points. The result is displayed in Fig. 14 and two important features can be observed: the existence of a secondary minimum around the abscissa ∼0.13 and a rise of the function after an apparent absolute minimum around ∼0.68. Concerning the first local minimum, a traveltime computation in the corresponding model shows that the maximum error with respect to data is 5.42×10^{-2} ms for the 180° acquisition geometry; this corresponds to a 18.45 kHz time period of the signal, which is close to our lowest inverted frequency. We therefore interpret this secondary minimum as a clear effect of cycle skip. The second minimum of the function corresponds to a model which happens to be very close to the model found before the final traveltime inversion we performed (Fig. 11b) and it could be schematically considered that the remaining models of the family (from 0.68 to 1) correspond to a part of model space that was explored during this second pass of traveltime tomography. Hence, just as a drop of the waveform misfit function had been achieved at the expense of the kinematic agreement, an improvement of traveltime fitting appears to be unfavourable to waveform fitting in a certain extent. Theoretically, the problem is physically consistent and both traveltime and waveform fitting should be achieved concomitantly. Yet, this is not what is being observed and two explanations can be proposed for this.

(1) Modelling errors could affect waveform tomography results. For wide-angle data in particular, phase conversions are likely to happen and are not taken into account by the acoustic modelling scheme. Neither is the possible effect of anelastic attenuation in the scatterers (particularly the lava cylinder), though their relatively small size with respect to the wavelengths of the signal should limit the problem. Also in this category of waveform modelling errors are the already mentioned source and receiver slight positioning discrepancies that result from the mismatch between the Cartesian modelling grid and the circular acquisition geometry. The source directivity is probably still a difficulty though its main effects were addressed in the way explained in the pre-processing paragraph. Finally, the amplitude discrepancy between 2.5-D real data and 2-D computed data is a well-known cause of error for waveform fitting issues even if approximate corrections exist (see Williamson & Pratt 1995 for a review).

(2) Possible traveltime picking errors could affect the consistency of the problem. Great care was taken in picking first arrivals but the weak amplitude of transmitted signals make such errors likely to happen. We consider the maximum error on our picked arrival times to be $\sim 8.00 \times 10^{-3}$ ms, which would lead to a maximum velocity error of ~ 500 m s^{-1} to be distributed among the two scatterers.

Considering the contradictory indications given by traveltime and waveform misfit, one could wonder which of the models in Figs 11(b) and (c) should be preferred. We rather favour the latter for two reasons:

(1) traveltime tomography is widely known to be more robust than waveform tomography and, apart from possible picking errors, its result can be trusted;

(2) the second traveltime tomography pass yields a better agreement with what is known from the scatterers, although this knowledge is only approximate.

Beyond that, both models give a precise image of the positions and shapes of the scatterers as well as a realistic estimation of their velocities.

7 CONCLUSIONS

In this study of a highly non-linear tomographic problem, we saw how traveltime and waveform approaches could be combined to retrieve the characteristics of the searched model, starting from the minimal state of information: the background. The non-linearity of the waveform fitting problem with respect to the low wavenumbers of the model is clearly illustrated when data are inverted with this technique only. The problem is classically addressed by defining a kinematically constrained and poorly resolved model with the help of traveltime tomography.

Starting from this model, waveform tomography converges towards a significantly better focused image of the scatterers. However, non-linearity appears not to be completely overcome and the kinematic agreement of traveltime tomography is not kept during the subsequent waveform inversion, possibly due to an inaccurate waveform modelling (of wide-angle scattered waves in particular) and, to a lesser extent, to traveltime picking errors. Concerning the former aspect, an effort to account for more physical properties of materials in both, modelling and inverting waveforms, is a potentially critical aspect and a clear direction for future developments.

A second pass of traveltime inversion allows one to re-improve the kinematic fitting while keeping the high resolution brought by

waveform tomography. Therefore, we see how such a dual approach of the tomographic inverse problem can mitigate its non-linearity. The concomitant use of two different tomographic tools could help in reaching areas of the model space that none of them, taken independently, would access, either for non-linearity or intrinsic limitations. We also see how this approach could help in addressing the problem of somewhat inaccurate modelling by one or both methods, though a natural solution would rather consist in further developing these tools, as mentioned just above for our frequency-domain waveform modelling.

Whether the strategy proposed here could be extended to surface or cross-well seismic experiments and what benefit could be drawn from this are open questions that are worth investigation.

ACKNOWLEDGMENTS

Patrick Amestoy (ENSEEIHT-IRIT, Toulouse, France) was of invaluable help in the development of our waveform modelling tool. He provided us with the linear solver he developed (Ma41 from the Harwell Subroutine Library), much advice and great active assistance in using it efficiently. The traveltime tomography code used in this study was written by Stéphane Operto and Céline Ravaut (UMR Géosciences Azur, Villefranche-sur-Mer, France), whom we thank very much for their help. We also thank Ginette Saracco, Frédéric Conil and Dominique Gibert (Laboratoire de géosciences, Rennes, France) for welcoming us and making the diffraction tomography experiment possible. Fruitful discussions with Gilles Lambaré, Mark Noble (ENSMP, Fontainebleau, France), Jean Virieux (Université de Nice, Sophia Antipolis, France) and Yann-Hervé de Rœck (IFREMER and IRISA, Rennes, France) were an appreciable help and an important source of inspiration. Some of the numerous tests we performed for this paper were carried out on the NEC-SX5 vector computer of IDRIS (Orsay, France). We finally thank Gerhard Pratt and another anonymous reviewer for fruitful and stimulating comments that helped to improve this work.

REFERENCES

Amestoy, P.R., Davis, T.A. & Duff, I.S., 1996. An approximate minimum degree ordering algorithm, *SIAM J. Matrix Anal. Appl.,* **17,** 886–905.

Cary, P.W. & Chapman, C.H., 1988. Automatic 1-D waveform inversion of marine seismic refraction data, *Geophys. J. Int.,* **93,** 527–546.

Collino, F., 1997. Perfectly matched absorbing layers for the paraxial equations, *J. Comp. Phys.,* **131,** 164–180.

Crase, E., Pica, A., Noble, M., McDonald, J. & Tarantola, A., 1990. Robust elastic nonlinear waveform inversion: application to real data, *Geophysics,* **55,** 527–538.

Crase, E., Wideman, C., Noble, M. & Tarantola, A., 1992. Non-linear elastic waveform inversion of land seismic reflection data, *J. geophys. Res.,* **97,** 4685–4703.

Devaney, A.J., 1984. Geophysical diffraction tomography, *IEEE Trans. Geosci. Remote Sensing,* **GE-22,** 3–13.

Djikpesse, H. & Tarantola, A., 1999. Multiparameter l_1 norm waveform fitting: interpretation of Gulf of Mexico reflection seismograms, *Geophysics,* **64,** 1023–1035.

Forgues, E., Scala, E. & Pratt, R.G., 1998. High resolution velocity model estimation from refraction and reflection data, *Expanded Abstracts of the 68th SEG Annual Int. Meeting,* 1211–1214.

Gauthier, O., Virieux, J. & Tarantola, A., 1986. Two-dimensional nonlinear inversion of seismic waveforms: numerical results, *Geophysics,* **51,** 1387–1403.

George, A. & Liu, J.W., 1981. *Computer Solution of Large Sparse Positive Definite Systems*, Prentice-Hall, Englewood Cliffs.

Greenspan, M. & Tschiegg, C.E., 1959. Tables of the speed of sound in water, *J. Acoust. Soc. Amer.,* **31,** 75–76.

Hicks, G.J., 2002. Arbitrary source and receiver positioning in finite-difference schemes using Kaiser windowed sinc functions, *Geophysics,* **67,** 156–165.

Hicks, G.J. & Pratt, R.G., 2001. Reflection waveform inversion using local descent methods: estimating attenuation and velocity over a gas-sand deposit, *Geophysics,* **66,** 598–612.

Hole, J.A. & Zelt, B.C., 1995. 3-D finite-difference reflection traveltimes, *Geophys. J. Int.,* **121,** 427–434.

Igel, H., Djikpesse, H. & Tarantola, A., 1996. Waveform inversion of marine reflection seismograms for, *P* impedance and Poisson's ratio, *Geophys. J. Int.,* **124,** 363–371.

Jin, S. & Madariaga, R., 1993. Background velocity inversion with a genetic algorithm, *Geophys. Res. Lett.,* **20,** 93–96.

Jo, C.H., Shin, C. & Suh, J.H., 1996. An optimal nine-point finite-difference frequency-space 2-D acoustic wave extrapolator, *Geophysics,* **61,** 529–537.

Kjartansson, E., 1979. Constant, *Q*-wave propagation and attenuation, *J. geophys. Res.,* **84,** 4737–4748.

Kolb, P., Collino, F. & Lailly, P., 1986. Prestack inversion of a 1-D medium, Special issue on seismic inversion, *Proc. IEEE,* **64,** 498–508.

Lailly, P., 1984. The seismic inverse problem as a sequence of before stack migrations, in *Inverse Scattering Theory and Application*, eds Bednar, J.B., Robinson, E. & Weglein, A., SIAM, Philadelphia.

Ludwig, W.F., Nafe, J.E. & Drake, C.L., 1970. Seismic refraction, in *The Sea*, Vol. 4, pp. 53–84, ed. Maxwell, A.E., Wiley-Interscience, New York.

Marfurt, K.J., 1984. Accuracy of finite-difference and finite-element modeling of the scalar and elastic wave-equations, *Geophysics,* **49,** 533–549.

Min, D.-J., Shin, C., Kwon, B.-D. & Chung, S., 2000. Improved frequency-domain elastic wave modeling using weighted-averaging difference operators, *Geophysics,* **63,** 289–296.

Mora, P., 1987. Nonlinear two-dimensional elastic inversion of multi-offset seismic data, *Geophysics,* **52,** 1211–1228.

Mora, P., 1988. Elastic wave-field inversion of reflection and transmission data, *Geophysics,* **53,** 750–759.

Pratt, R.G., 1990. Frequency domain elastic wave modeling by finite-differences: a tool for crosshole seismic imaging, *Geophysics,* **55,** 626–632.

Pratt, R.G., 1999. Seismic waveform inversion in the frequency domain, Part 1: Theory and verification in a physical scale model, *Geophysics,* **64,** 888–901.

Pratt, R.G. & Goulty, N.R., 1991. Combining wave-equation imaging with traveltime tomography to form high resolution images from crosshole data, *Geophysics,* **56,** 208–224.

Pratt, R.G. & Shipp, R.M., 1999. Seismic waveform inversion in the frequency domain, Part 2: Fault delineation in sediments using crosshole data, *Geophysics,* **64,** 902–914.

Pratt, R.G. & Worthington, M.H., 1988. The application of diffraction tomography to cross-hole seismic data, *Geophysics,* **53,** 1284–1294.

Pratt, R.G. & Worthington, M.H., 1990. Inverse theory applied to multi-source cross-hole tomography: Part 1, Acoustic wave-equation method, *Geophys. Prospect.,* **38,** 287–310.

Pratt, R.G., Song, Z.-M., Williamson, P.R. & Warner, M., 1996. Two-dimensional velocity models from wide-angle seismic data by wavefield inversion, *Geophys. J. Int.,* **124,** 323–340.

Pratt, R.G., Shin, C. & Hicks, G., 1998. Gauss–Newton and full Newton methods in the frequency-space seismic waveform inversion, *Geophys. J. Int.,* **133,** 341–362.

Press W.H., Teukolsky, S.A., Vettering, W.T. & Flannery, B.P., 1992. *Numerical Recipes in Fortran 77: the Art of Scientific Computing*, 2nd edn, Cambridge University Press, New York.

Ribodetti, A., Operto, S., Virieux, J., Lambaré, G., Valéro, H.-P. & Gibert, D., 2000. Asymptotic viscoacoustic diffraction tomography of ultrasonic laboratory data: a tool for rock properties analysis, *Geophys. J. Int.,* **140,** 324–340.

Sambridge, M. & Drijkoningen, G., 1992. Genetic algorithms in seismic waveform inversion, *Geophys. J. Int.,* **109,** 323–342.

Saracco, G., Ribodetti, A., Turquety, S. & Conil, F., 2000. Ultasonic seismic imaging of lava samples by viscoacoustic asymptotic waveform

inversion: calibration and developments, *Proc. 17th IEEE Instrumentation and Measurement Technology Conf.,* pp. 380–385.

Sen, M.K. & Stoffa, P.L., 1992. Rapid sampling of model space using genetic algorithms: examples from seismic waveform inversion, *Geophys. J. Int.,* **108,** 281–292.

Shin, C. & Sohn, H., 1998. A frequency-space 2-D scalar wave extrapolator using extended 25-point finite-difference operator, *Geophysics,* **63,** 289–296.

Slaney, M., Kak, A.C. & Larsen, L.E., 1984. Limitations of imaging with first-order diffraction tomography, *IEEE Trans. Microwave Theory Techn.,* **MTT-32,** 860–874.

Song, Z.-M., Williamson, P.R. & Pratt, R.G., 1995. Frequency-domain acoustic wave modeling and inversion of cross-hole data: Part II—Inversion method, synthetic experiments and real data results, *Geophysics,* **60,** 796–809.

Šteckl, I., 1998. Frequency domain seismic forward modelling: a tool for waveform inversion, *PhD thesis*, Imperial College of science, Technology and Medicine, University of London.

Šteckl, I. & Pratt, R.G., 1998. Accurate viscoelastic modeling by frequency-domain finite differences using rotated operators, *Geophysics,* **63,** 1779–1794.

Tarantola, A., 1984. Inversion of seismic reflection data in the acoustic approximation, *Geophysics,* **49,** 1259–1266.

Tarantola, A., 1986. A strategy for nonlinear elastic inversion of seismic reflection data, *Geophysics,* **51,** 1893–1903.

Tarantola, A., 1987. *Inverse Problem Theory: Methods for Data Fitting and Model Parameter Estimation*, Elsevier, Amsterdam.

Tarantola, A., 1988. Theoretical background for the inversion of seismic waveforms including elasticity and attenuation, *Pure appl. Geophys.,* **128,** 365–399.

Toomey, D.R., Solomon S.C. & Purdy, G.M., 1994. Tomographic imaging of the shallow crustal structure of the East Pacific Rise at 9°30′N, *J. geophys. Res.,* **99,** 24 135–24 157.

Valéro, H.-P., 1997. Endoscopie sismique, *PhD thesis,* Institut de Physique du Globe de Paris.

Williamson, P.R., 1991. A guide to the limits of resolution imposed by scattering in ray tomography, *Geophysics,* **56,** 202–207.

Williamson, P.R. & Pratt, R.G., 1995. A critical review of acoustic wave modeling procedures in 2.5 dimensions, *Geophysics,* **60,** 591–595.

Wu, R. & Toksöz, M.N., 1987. Diffraction tomography and multi-source holography applied to seismic imaging, *Geophysics,* **52,** 11–25.

Xia, G., Sen, M.K. & Stoffa, P.L., 1998. 1-D elastic waveform inversion: a divide-and-conquer approach, *Geophysics,* **63,** 1670–1684.

Zelt, C.A. & Barton, P.J., 1998. Three-dimensional seismic refraction tomography: a comparison of two methods applied to data from the Faeroe Basin, *J. geophys. Res.,* **103,** 7187–7210.

Zhou, C., Cai, W., Luo, Y., Schuster, G.T. & Hassanzadeh, S., 1995. Acoustic wave-equation traveltime and waveform inversion of crosshole seismic data, *Geophysics,* **60,** 765–773.

Zhou, C., Schuster, G.T., Hassanzadeh, S. & Harris, J.M., 1997. Elastic wave equation traveltime and waveform inversion of crosswell data, *Geophysics,* **62,** 853–868.